

## SPECTROSCOPY

# Real-space imaging of anisotropic charge of $\sigma$ -hole by means of Kelvin probe force microscopy

B. Mallada<sup>1,2,3,†</sup>, A. Gallardo<sup>2,4,†</sup>, M. Lamanec<sup>3,5,†</sup>, B. de la Torre<sup>1,2</sup>, V. Špirko<sup>5,6</sup>, P. Hobza<sup>5,7,\*</sup>, P. Jelinek<sup>1,2,\*</sup>

An anisotropic charge distribution on individual atoms, such as  $\sigma$ -holes, may strongly affect the material and structural properties of systems. However, the spatial resolution of such anisotropic charge distributions on an atom represents a long-standing experimental challenge. In particular, the existence of the  $\sigma$ -hole on halogen atoms has been demonstrated only indirectly through the determination of the crystal structures of organic molecules containing halogens or with theoretical calculations, consequently calling for its direct experimental visualization. We show that Kelvin probe force microscopy with a properly functionalized probe can image the anisotropic charge of the  $\sigma$ -hole and the quadrupolar charge of a carbon monoxide molecule. This opens a new way to characterize biological and chemical systems in which anisotropic atomic charges play a decisive role.

The observation of molecular structures with the unusual atomic arrangement of possessing two adjacent halogens or a pair of halogen atoms and electron donor motifs (oxygen, nitrogen, sulfur, ...), found in different crystals in the second half of the 20th century (1–4), represented a long-standing puzzle in supramolecular chemistry. Both halogens and electron donors are electronegative elements that carry a negative charge. Thus, close contacts of these atoms should theoretically cause highly repulsive electrostatic interaction. Counterintuitively, such atoms are frequently found to form intermolecular bonds, called latter halogen bonds, that stabilize the molecular crystal structure. An elegant solution offered by Auffinger *et al.* (5), Clark *et al.* (6), and Politzer *et al.* (7, 8) showed that the formation of a covalent bond between certain halogen atoms (chlorine, bromine, and iodine) and a more electronegative atom (such as carbon) gives rise to a so-called  $\sigma$ -hole that has an anisotropic charge distribution on the halogen atom. Thus, a physical observable corresponding electrostatic potential around the halogen atom is not uniform (as considered within all empirical force fields) but exhibits an electropositive distal to covalently bound carbon

crown surrounded by an electronegative belt (Fig. 1A).

Consequently, halogen bonding is attributed to attractive electrostatic interaction between a halogen's electropositive  $\sigma$ -hole and an electronegative belt of the other halogen or an electronegative atom with negative charge. The International Union of Pure and Applied Chemistry (IUPAC) definition of a halogen bond (9) states that a halogen bond “occurs when there is evidence of a net attractive interaction between an electrophilic region associated with a halogen atom in a molecular entity and a nucleophilic region in another, or the same, molecular entity.” Stability of the  $\sigma$ -hole bonding is comparable with that of hydrogen-bonded complexes, and attraction in both types of noncovalent complexes was originally assigned to electrostatic interaction. Although this scenario is basically true for H-bonded complexes, in the case of halogen-bonded systems, the importance of dispersion interaction (10) was highlighted. The importance of the dispersion interaction is not surprising because close contact takes place between two heavy atoms with high polarizability in halogen-bonded complexes.

The concept of halogen bonding was later generalized to a  $\sigma$ -hole bonding concept. In particular, the halogen (group 17), chalcogen (group 16), pnictogen (group 15), tetrel (group 14), and aerogen bonding (group 18) were established according to the name of the electronegative atom bearing the positive  $\sigma$ -hole. The existence of a  $\sigma$ -hole in atoms of the mentioned groups of elements has a common origin in the unequal occupation of valence orbitals.

The  $\sigma$ -hole bonding plays a key role in supramolecular chemistry (11), including the engineering of molecular crystals or in biological macromolecular systems (5). Despite its relevance and intensive research devoted to  $\sigma$ -hole bonding, the existence of the  $\sigma$ -hole itself was confirmed only indirectly with quantum calcu-

lations (5–8) or crystal structures of complexes containing  $\sigma$ -hole donors and electron acceptors (11–15). However, a direct visualization of this entity allowing for the resolution of its peculiar shape has thus far been missing.

The cause of the  $\sigma$ -hole is the anisotropic distribution of the atomic charge on a halogen atom. The imaging of anisotropic atomic charge represents an unfulfilled challenge for experimental techniques, including scanning probe microscopy (SPM), electron microscopy, and diffraction methods. Thus, we sought a technique in which the imaging mechanism relies on the electrostatic force to facilitate the visualization of the anisotropic charge distribution on a halogen atom with a sub-ångström spatial resolution. We show that real-space visualization of the  $\sigma$ -hole can be achieved through Kelvin probe force microscopy (KPFM) under ultrahigh vacuum (UHV) conditions (16, 17) with unprecedented spatial resolution.

KPFM belongs to a family of SPM techniques that routinely provide real-space atomic resolution of surfaces. In the KPFM technique, the variation of the frequency shift  $\Delta f$  of an oscillating probe on applied bias voltage  $V$  with the quadratic form  $\Delta f \sim V^2$  is recorded (18). The vertex of the Kelvin parabola  $\Delta f(V)$  determines the difference between work functions of tip and sample, also called the contact potential difference  $V_{CPD}$ . Moreover, the spatial variation of the contact potential difference  $V_{CPD}$  across the surface allows the mapping of local variation of surface dipole on the sample ( $V_{LCDP}$ ) (17). Recent developments of the KPFM technique operating in UHV conditions made it possible to reach true atomic resolution on surfaces (19, 20) to image intramolecular charge distribution (21), to control single-electron charge states (22), to resolve bond polarity (23), or to discriminate charge (24).

The atomic contrast in KPFM images originates from a microscopic electrostatic force between static ( $\rho_0$ ) and polarized charge densities ( $\delta\rho$ ) located on frontier atoms from the tip apex and sample when an external bias is applied (17). There are two dominant components of this force: the interaction between the polarized charge on the apex  $\delta\rho_t$ , which is linearly proportional to the applied bias voltage ( $V$ ), and the static charge on sample  $\rho_s^0$ . The second term consists of the electrostatic interaction between the polarized charge on the sample  $\delta\rho_s$  and the static charge on tip  $\rho_t^0$ . Consequently, these two components cause local variation of the contact potential difference  $V_{LCDP}$  (a detailed description of the mechanism is provided in the supplementary materials), thus providing atomic-scale contrast.

## Results

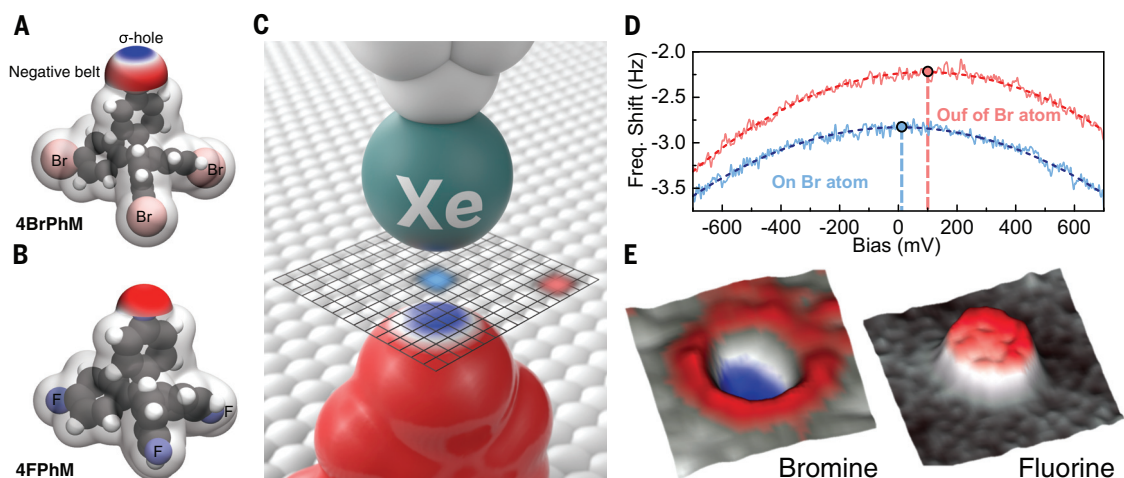
Consequently, KPFM appears to be the tool of choice for imaging anisotropic charge distribution within a single atom, such as the

<sup>1</sup>Regional Centre of Advanced Technologies and Materials, Czech Advanced Technology and Research Institute (CATRIN), Palacký University Olomouc, 78371 Olomouc, Czech Republic. <sup>2</sup>Institute of Physics, Academy of Sciences of the Czech Republic, Prague, Czech Republic. <sup>3</sup>Department of Physical Chemistry, Palacký University Olomouc, tr. 17. listopadu 12, 771 46 Olomouc, Czech Republic. <sup>4</sup>Department of Condensed Matter Physics, Faculty of Mathematics and Physics, Charles University, V Holešovičkách 2, 180 00 Prague, Czech Republic. <sup>5</sup>Institute of Organic Chemistry and Biochemistry, Czech Academy of Sciences, Flemingovo Náměstí 542/2, 16000 Prague, Czech Republic. <sup>6</sup>Department of Chemical Physics and Optics, Faculty of Mathematics and Physics, Charles University in Prague, Ke Karlovu 3, 12116 Prague, Czech Republic. <sup>7</sup>IT4Innovations, VSB-Technical University of Ostrava, 17. listopadu 2172/15, 70800 Ostrava-Poruba, Czech Republic.

\*Corresponding author. Email: pavel.hobza@uochb.cas.cz (P.H.); jelinekp@fzu.cz (P.J.)

†These authors contributed equally to this work.

**Fig. 1. Schematic view of the KPFM measurements to image a  $\sigma$ -hole.** (A and B) Models of 4BrPhM and 4FPhM molecules, including corresponding electrostatic potential map on outermost Br/F atom. They reveal the presence of the  $\sigma$ -hole on a Br atom, and there is an isotropic negative charge on the F atom. (C) Schematic view of the acquisition method of the KPFM measurement with a functionalized Xe-tip on a 2D grid. (D) Corresponding  $\Delta f(V)$  parabolas acquired in the central part (blue) of the 2D grid and on the periphery (red). Vertical dashed lines indicate the value of  $V_{\text{LCPD}}$  for the given  $\Delta f(V)$  parabola, which forms the 2D KPFM image. (E) 3D representation of the KPFM images ( $V_{\text{LCPD}}$  maps) acquired with an Xe-tip over bromide and fluoride atoms of 4BrPhM and 4FPhM molecules. Blue indicates low values of  $V_{\text{LCPD}}$ , and red indicates high values of  $V_{\text{LCPD}}$ .



$\sigma$ -hole. To test this hypothesis, we deliberately chose tetrakis(4-bromophenyl) methane (4BrPhM) and tetrakis(4-fluorophenyl) methane (4FPhM) compounds (Fig. 1, A and B). The skeleton arrangement of these compounds facilitates a tripodal configuration once deposited onto a surface with a single bromine-fluorine atom oriented outward from the surface (fig. S1). This arrangement facilitated direct inspection of the  $\sigma$ -hole on a halogen atom by the front-most atom of a scanning probe, (Fig. 1C). Deposition of the molecules in low coverage (less than 1 monolayer) on the Ag(111) surface held at room temperature under UHV conditions led to the formation of well-ordered, self-assembled molecular arrangements in a rectangular formation (Fig. 2, A and B). Bromine atoms of the 4BrPhM molecule have a substantial positive  $\sigma$ -hole (Fig. 1A), and fluorine atoms possess an isotropic negative charge (Fig. 1B). This enabled us to perform comparative measurements on similar systems with and without the presence of the  $\sigma$ -hole.

Shown in Fig. 2, C and D, is a substantial contrast between two-dimensional (2D) constant-height KPFM maps acquired over Br and F front-most atoms of the molecular compounds with an Xe-decorated tip. In the case of the 4FPhM molecule, we observed a monotonous elliptical increase of the  $V_{\text{LCPD}}$  signal over the fluorine atom. In comparison, the KPFM image over the 4BrPhM molecule featured a notable ring-like shape. The 2D KPFM maps were recorded in the attractive tip-sample interaction regime near the minimum of the  $\Delta f$ - $z$  curve (fig. S2) to avoid undesired topographic cross-talk (fig. S3 and supplementary text) or the effect of lateral bending of the functionalized probe due to repulsive forces (25) that could cause image distortions. Evolution of the contrast of the KPFM image of the  $\sigma$ -hole

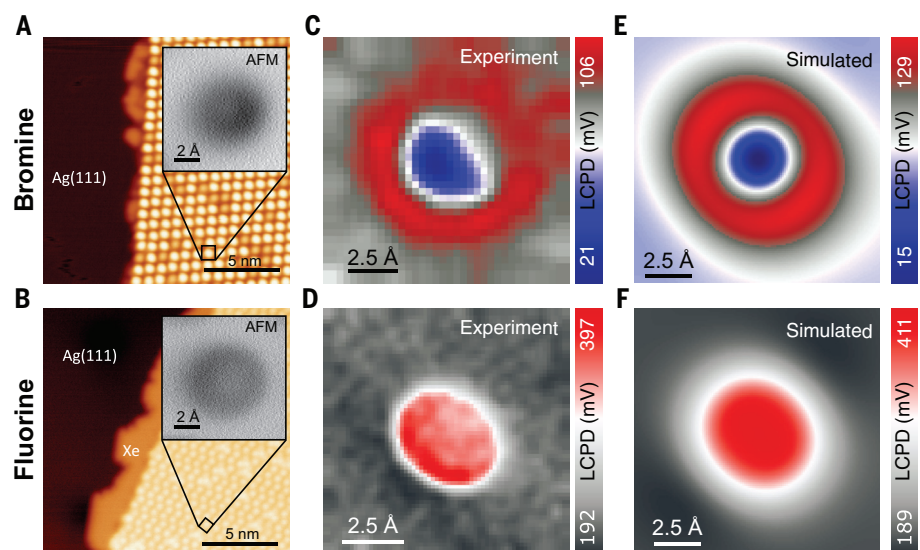


**Fig. 2. KPFM imaging of 4BrPhM and 4FPhM molecules with an Xe-tip.** (A and B) STM images of a molecular self-assembled submonolayer of 4BrPhM and 4FPhM molecules on an Ag(111) surface. (Insets) AFM images acquired on a single molecule with a Xe tip at the minima of the frequency shift. (C and D) Experimental KPFM images obtained with a functionalized Xe tip over bromide and fluoride atoms of single 4BrPhM and 4FPhM molecules. (E and F) Calculated KPFM images with a functionalized Xe tip of single 4BrPhM and 4FPhM molecules. Blue indicates low values of  $V_{\text{LCPD}}$  and red indicates high values of  $V_{\text{LCPD}}$ .

on the front-most Br atom with the tip-sample distance is shown in fig. S4.

## Discussion

To confirm the origin of the anisotropic contrast observed experimentally on the Br atom, we carried out KPFM simulations using static  $\rho_0$  and polarized  $\delta\rho$  charges of Br and F-terminated molecules and Xe-tip models obtained from density functional theory (DFT) calculations (fig. S5). Simulated KPFM maps that are perfectly matched to the experimental

maps are shown in Fig. 2, E and F. Our theoretical model allowed us to decompose the two leading contributions: the electrostatic interaction of the polarized charge on tip  $\delta\rho_t$  with the static charge on the molecule and the counterpart term of the electrostatic interaction between the polarized charge on molecule  $\delta\rho_s$  with the  $\rho_t^0$  static charge of the tip (fig. S5). We found that the anisotropic contrast obtained on the Br-terminated molecule can be rationalized from a variation of the microscopic electrostatic interaction between



atomic-scale charges of tip and sample. On the periphery of the Br atom, the positive shift of  $V_{\text{CPD}}$  is given by the electrostatic interaction of the spherical polarized charge,  $\delta\rho_t$  of the Xe-tip apex, with the belt of negative charge surrounding the positive  $\sigma$ -hole. By contrast, in the central part, the electrostatic interaction with the positive crown of the  $\sigma$ -hole turned the  $V_{\text{LCPD}}$  value with respect to that on the peripheral region. In the case of the 4FPhM molecule, both terms provided a trivial contrast with a positive shift of the  $V_{\text{LCPD}}$  over the atom. The term corresponding to the static charge  $\rho_s^0$  on the molecule revealed an elliptical shape originating from neighbor positively charged hydrogen atoms in the underlying phenyl group of the 4FPhM molecule. Therefore, the shape of the feature presented in the KPFM image provided additional information about the internal arrangement of the molecule on the surface.

We deliberately used a single Xe atom to functionalize the tip apex instead of the more commonly used carbon monoxide (CO). As discussed above, the Xe tip allowed us to optimize the imaging conditions of the  $\sigma$ -hole because static charge density  $\rho_0$  on the apex of the CO-tip had a strong quadrupolar character (Fig. 3A), and the charge on the Xe tip was highly spherical (fig. S5). This choice eliminated spurious spatial variation of the  $V_{\text{LCPD}}$  signal, which did not belong directly to the  $\sigma$ -hole. In particular, a component of the microscopic electrostatic interaction between static charge  $\rho_t^0$  of the tip and polarized charge on sample  $\delta\rho_s$  needs to be abolished. In the case of the Xe-tip, the spatial variation of the local  $V_{\text{CPD}}$  was dominated by the component that includes the interaction of a spherically polarized charge on the Xe atom  $\delta\rho_t$  with the anisotropic electrostatic field of the  $\sigma$ -hole. This enabled a direct mapping of the spatial charge distribution of the  $\sigma$ -hole by means of the KPFM technique.

Thus, it is instructive to look at the KPFM images acquired with the CO tip on the 4FPhM molecule as well. Despite the frontier fluorine atom of the 4FPhM molecule having an isotropic charge distribution, the experimental KPFM image (Fig. 3B) features a nontrivial ringlike shape with lower values of the  $V_{\text{LCPD}}$  signal on the center of the fluorine atom. Our KPFM simulation using a CO-tip (Fig. 3C) coincided qualitatively with the experimental counterpart. From a detailed analysis of the electrostatic components (fig. S6), we found that the contrast arose from the interaction of the spherical polarized charge  $\delta\rho_s$  on a fluorine atom with the static quadrupole charge on a CO tip, composed of a negative crown of density on an oxygen atom surrounded by a positive charge belt (Fig. 3A). Thus, the KPFM features resolved on the 4FPhM molecule re-

flected the quadrupolar charge distribution of the CO tip. Thus, from the spatial variation of the  $V_{\text{LCPD}}$  signal, we could determine the sign of the quadrupole of the CO molecule on the tip. The shift of  $V_{\text{LCPD}}$  toward lower values in the central part of the KPFM image was caused by the negative charge crown of the quadrupole charge localized at oxygen (Fig. 3A). The enhanced  $V_{\text{LCPD}}$  value on the periphery reflects the positively charged belt of the quadrupole charge of the CO molecule. This reverse shift of  $V_{\text{LCPD}}$  with respect to the previous case of the  $\sigma$ -hole was caused by our inspection of the anisotropic charge on the tip instead of the sample. A detailed explanation of the origin and sign of  $V_{\text{LCPD}}$  shift is available in the supplementary materials.

Alternatively, some works reported subatomic features in noncontact atomic force microscopy (nc-AFM) (26) images with CO functionalized tips (27). However, the origin of such contrast and their interpretation of the physical meaning are under debate (28, 29). Additionally, nc-AFM has demonstrated unprecedented chemical resolution of single molecules (30) or their charge distribution (31). Thus, we were intrigued by the possibility of imaging the  $\sigma$ -hole by means of nc-AFM with functionalized tips (27).

A series of high-resolution nc-AFM images acquired at a wide range of tip-sample distances are shown in fig. S7 with a CO tip and Xe tip, respectively. At the onset of the atomic contrast in nc-AFM mode, the tip-sample interaction was dominated by an attractive dispersion. The resulting AFM contrast for both 4FPhM and 4BrPhM molecules had a similar spherical character that lacks any subatomic feature. Also, in close tip-sample distances, the AFM contrast remained similar for both molecular compounds, featuring a bright spot in the center caused by the Pauli repulsion. Thus, we found that the AFM images did not

reveal any signature of the  $\sigma$ -hole in the whole range of tip-sample distances covering both an attractive and repulsive interaction regime.

To understand in detail this experimental observation, we performed theoretical analysis of the nc-AFM images with a CO tip using the probe particle SPM model (25). Shown in figs. S8 and S9 are lateral cross sections of different force components of the interaction energy acting between the CO tip and the outermost F and Br atoms of the 4FPhM and 4BrPhM molecules, respectively. The calculated AFM images showed similar atomic contrast, ruling out the possibility to image the  $\sigma$ -hole with a CO tip. From the analysis, we inferred that the AFM contrast was dominated by dispersive and Pauli interaction, both of which have a highly spherical character. On the other hand, the electrostatic interaction possesses an anisotropic character caused by the presence of both a  $\sigma$ -hole on the Br atom and a quadrupolar charge distribution on the apex of the CO-tip (Fig. 3A). Nevertheless, the magnitude of the electrostatic interaction was about one order smaller than the competing dispersion and Pauli interactions, which made the  $\sigma$ -hole hard to image in the AFM technique. From this analysis, we could conclude that the resolution of anisotropic atomic charges requires a technique such as KPFM, whose contrast mechanism is mastered by the electrostatic interaction that maps the charge distribution on the forefront atoms.

Next, we investigated the influence of the  $\sigma$ -hole on the noncovalent intermolecular interaction energies. The nc-AFM technique provided the distinctive possibility to explore interaction energies between individual atoms and molecules placed on the tip apex and sample by means of site-specific force spectroscopies (32–35). Apart from a quantitative evaluation of the interaction energies between well-defined entities, the nc-AFM

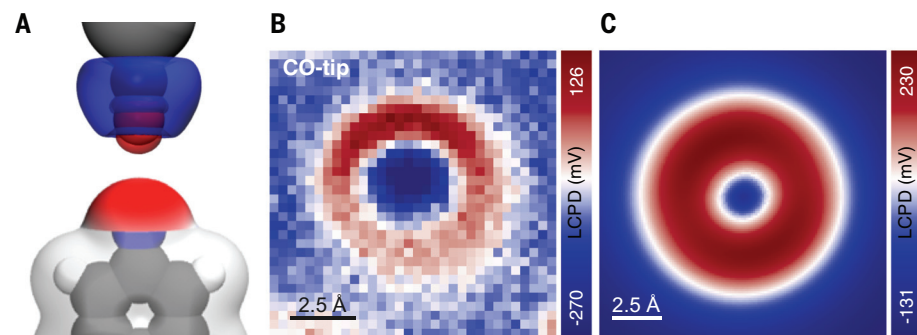


**Fig. 3. KPFM imaging of a 4FPhM molecule with a CO tip.** (A) Schematic view of a CO tip above a 4FPhM molecule with a superimposed calculated differential charge density of the CO tip, revealing (top) a quadrupole charge of a CO-tip model and (bottom) calculated electrostatic potential of 4FPhM molecule showing an isotropic negative charge on the frontier fluorine atom in 4FPhM. (B) Experimental KPFM image acquired over the frontier fluorine atom with a CO tip. (C) Simulated KPFM image of a 4FPhM molecule with a CO tip. Blue indicates low values of  $V_{\text{LCPD}}$ , and red indicates high values of  $V_{\text{LCPD}}$ .

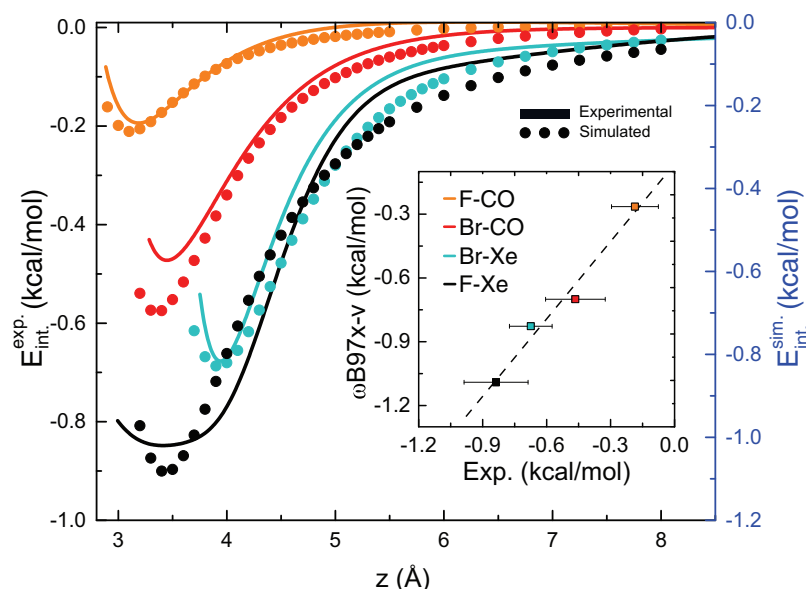


**Fig. 4.** Comparison of experimental and theoretical interaction energies of four complexes. Experimental (solid curves) and calculated (dots, obtained with DFT/ $\omega$ B97X-V) energy curves versus tip-sample distance between 4FPhM and 4BrPhM molecules and Xe and CO tips. (Inset) The correlation between experimental and theoretical values [coefficient of determination ( $R^2$ ) = 0.98] of the energy minima for all complexes. Bars indicate an estimated experimental error of the energy minima calculated as the difference between a polynomial fit and the experimental energy (fig. S12).

technique also gave an invaluable opportunity to benchmark the accuracy of different theoretical methods to describe these weak noncovalent interactions (34–36).

Tip functionalization offered an opportunity to explore distinct scenarios of the interaction mechanisms with molecular complexes. The Xe tip has a positive net charge and large polarizability, but the CO tip possesses a quadrupolar charge (O and C carry negative and positive net charge, respectively) and a relatively small polarizability. Their interaction energies are shown in Fig. 4, with the 4FPhM and 4BrPhM molecules as a function of the tip-sample distance. Small values of the maximum energies of 0.2 to 0.83 kcal/mol revealed a noncovalent bonding mechanism. In general, the complexes with an Xe-tip are more stable than the complexes with a CO tip, which may be rationalized by a larger dispersion interaction caused by an Xe tip. We observed that the Xe-4BrPhM complex was less stable than the Xe-4FPhM complex (by 0.67 and 0.83 kcal/mol, respectively) despite the larger polarizability of Br that determines the magnitude of the polarization interaction. This effect was caused by the presence of the repulsive electrostatic interaction between the positive  $\sigma$ -hole on a Br atom and the positively charged Xe tip, which partially cancelled the attractive dispersive interaction in the Xe-4BrPhM complex. On the other hand, the dispersive and electrostatic forces are both attractive in the case of the Xe-4FPhM complex, resulting

in a larger total interaction energy. This observation not only supported the presence of the positive  $\sigma$ -hole on the Br atom, it also explained the origin of a peculiar intermolecular orientation of halogen-bonded molecular systems (12–15).

Recently, a vigorous effort has been devoted to the development of computational methods based on DFT with dispersion correction that are able to reliably describe intermolecular interactions in noncovalent complexes (37). But their transferability is still limited owing to adopted approximations, and thus, careful benchmarking is desired. From this perspective, the above-described complexes represent interesting noncovalent systems for benchmarks with a complex interplay between the dispersion and the electrostatic interaction. The maximum interaction energies measured were below 1 kcal/mol, which used to be considered as the limit of chemical accuracy, further strengthening the benchmark.

Accurate interaction energies for different types of noncovalent complexes could be obtained from a nonempirical coupled-cluster method covering triple-excitations [CCSD(T)]. Unfortunately, its large computational demands made it impossible to apply this method to a system of the size of the molecules we investigated in the present work.

To circumvent this problem, we performed the CCSD(T) calculations on smaller reference model systems consisting of F- and Br-benzene, exhibiting similar characteristics as

4BrPhM and 4FPhM molecules (supplementary materials). We compared the calculated CCSD(T) interaction energies to interaction energies obtained with several popular DFT functionals (table S3). We found that the range-separated  $\omega$ B97X-V functional (38) that implicitly covers dispersion energy provided good agreement with the benchmarked dataset (table S3). Because this functional was also shown to provide the best results among other popular DFT functionals for various types of systems with noncovalent interactions (38), we selected this functional for further use.

To check its transferability to our larger molecular systems, we calculated the interaction energies between 4FPhM and 4BrPhM molecules and Xe- and CO-tip models. Excellent agreement between the  $\omega$ B97X-V interaction energies and the experimental data results is shown in Fig. 4. The calculated energy minima for all complexes fit the measured values perfectly within the experimental error (Fig. 4, inset). The PBE0 functional (39) with the D3 correction (40) reproduced the CCSD(T) results on small-model systems as well (table S3 and fig. S10). However, its transferability on the large systems was no longer as good as the range-separated  $\omega$ B97X-V functional (fig. S11).

The  $\omega$ B97X-V functional describes well the interaction trend for all considered systems (Fig. 4, inset), with the caveat that it systematically slightly overestimates the interaction energy by  $\sim 0.1$  kcal/mol. The perfect agreement between theoretical and experimental values could not be expected because calculations were limited to free-standing 4FPhM and 4BrPhM molecules interacting with Xe- and CO-tip model, and in the experiment, 4FPhM and 4BrPhM molecules were adsorbed at Ag(111) surface. The results confirmed good transferability of the  $\omega$ B97X-V functional toward larger systems. Moreover, the good agreement between calculated and experimental datasets obtained for all four complexes also gave confidence in the multiscale benchmark technique that uses small-model complexes with the Xe-tip model. Therefore, this approach makes it possible to accurately describe systems whose size does not allow for the direct application of the accurate coupled-cluster technique (or a similar technique), or when other direct experimental measurements are currently not feasible.

## Conclusions

We report the possibility of achieving the spatial resolution of anisotropic atomic charge with the KPFM technique, which not only provided direct evidence of the existence of  $\sigma$ -holes but is expected to substantially extend the possibility to characterize charge distribution in complex molecular systems and on surfaces. We anticipate that this technique could

be further extended to provide invaluable information about the local inhomogeneous polarizability of individual atoms on surfaces or within molecules with unprecedented spatial resolution in chemical and biologically relevant systems.

## REFERENCES AND NOTES

- N. Ramasubbu, R. Parthasarathy, P. Murray-Rust, *J. Am. Chem. Soc.* **108**, 4308–4314 (1986).
- O. Hassel, J. Hvorslev, E. H. Vihovde, N. A. Sørensen, *Acta Chem. Scand.* **8**, 873–873 (1954).
- O. Hassel *et al.*, *Acta Chem. Scand.* **13**, 275–280 (1959).
- O. Hassel *et al.*, *Acta Chem. Scand.* **12**, 1146–1146 (1958).
- P. Auffinger, F. A. Hays, E. Westhof, P. S. Ho, *Proc. Natl. Acad. Sci. U.S.A.* **101**, 16789–16794 (2004).
- T. Clark, M. Hennemann, J. S. Murray, P. Politzer, *J. Mol. Model.* **13**, 291–296 (2007).
- T. Brinck, J. S. Murray, P. Politzer, *Int. J. Quantum Chem.* **44** (S19), 57–64 (1992).
- P. Politzer, P. Lane, M. C. Concha, Y. Ma, J. S. Murray, *J. Mol. Model.* **13**, 305–311 (2007).
- G. R. Desiraju *et al.*, *Pure Appl. Chem.* **85**, 1711–1713 (2013).
- K. E. Riley, P. Hobza, *Phys. Chem. Chem. Phys.* **15**, 17742–17751 (2013).
- L. C. Gilday *et al.*, *Chem. Rev.* **115**, 7118–7195 (2015).
- Z. Han *et al.*, *Science* **358**, 206–210 (2017).
- J. Tschakert *et al.*, *Nat. Commun.* **11**, 5630 (2020).
- S. Kawai *et al.*, *ACS Nano* **9**, 2574–2583 (2015).
- H. Huang *et al.*, *ACS Nano* **10**, 3198–3205 (2016).
- M. Nonnenmacher, M. P. O'Boyle, H. K. Wickramasinghe, *Appl. Phys. Lett.* **58**, 2921–2923 (1991).
- T. Glatzel, S. Sadewasser, Eds., *Kelvin Probe Force Microscopy* (Springer, 2018), vol. 65.
- W. Melitz, J. Shen, A. C. Kummel, S. Lee, *Surf. Sci. Rep.* **66**, 1–27 (2011).
- L. Nony, A. S. Foster, F. Bocquet, C. Loppacher, *Phys. Rev. Lett.* **103**, 036802 (2009).
- S. Sadewasser *et al.*, *Phys. Rev. Lett.* **103**, 266103 (2009).
- F. Mohn, L. Gross, N. Moll, G. Meyer, *Nat. Nanotechnol.* **7**, 227–231 (2012).
- L. Gross *et al.*, *Science* **324**, 1428–1431 (2009).
- F. Albrecht *et al.*, *Phys. Rev. Lett.* **115**, 076101 (2015).
- B. Mallada *et al.*, *ACS Sustain. Chem. Eng.* **8**, 3437–3444 (2020).
- P. Hapala *et al.*, *Phys. Rev. B Condens. Matter Mater. Phys.* **90**, 085421 (2014).
- T. R. Albrecht, P. Grütter, D. Horne, D. Rugar, *J. Appl. Phys.* **69**, 668–673 (1991).
- P. Jelínek, *J. Phys. Condens. Matter* **29**, 343002 (2017).
- F. Huber *et al.*, *Science* **366**, 235–238 (2019).
- M. Emmrich *et al.*, *Science* **348**, 308–311 (2015).
- L. Gross, F. Mohn, N. Moll, P. Liljeroth, G. Meyer, *Science* **325**, 1110–1114 (2009).
- P. Hapala *et al.*, *Nat. Commun.* **7**, 11560 (2016).
- M. A. Lantz *et al.*, *Science* **291**, 2580–2583 (2001).
- Y. Sugimoto *et al.*, *Nature* **446**, 64–67 (2007).
- S. Kawai *et al.*, *Nat. Commun.* **7**, 11559 (2016).
- Z. Sun, M. P. Boneschanscher, I. Swart, D. Vanmaekelbergh, P. Liljeroth, *Phys. Rev. Lett.* **106**, 046104 (2011).
- C. Wagner *et al.*, *Nat. Commun.* **5**, 5568 (2014).
- S. Grimme, A. Hansen, J. G. Brandenburg, C. Bannwarth, *Chem. Rev.* **116**, 5105–5154 (2016).
- N. Mardirossian, M. Head-Gordon, *Phys. Chem. Chem. Phys.* **16**, 9904–9924 (2014).
- A. Adamo, V. Barone, *J. Chem. Phys.* **110**, 6158–6170 (1999).
- S. Grimme, J. Antony, S. Ehrlich, H. Krieg, *J. Chem. Phys.* **132**, 154104 (2010).
- B. Mallada *et al.*, Data for “Real-space imaging of anisotropic charge of  $\sigma$ -hole by means of Kelvin probe force microscopy”. Zenodo (2020); doi:10.5281/zenodo.5172233.

## ACKNOWLEDGMENTS

We acknowledge fruitful discussions with A. Růžička and P. Hapala. M.L. acknowledges inspirational advice from his previous supervisor, J. Kuchár. P.J. and B.d.I.T. dedicate this manuscript to the memory of J. M. Gómez-Rodríguez. **Funding:** This work was supported by the Czech Science Foundation GACR 20-13692X (A.G., B.M., and P.J.) and 19-27454X (P.H.); Praemium Academie of the Academy of Science of the Czech Republic (A.G.); Palacký University Internal Grant Association IGA\_PrF\_2021\_031 (M.L.); Palacký University Internal Grant Association IGA\_PrF\_2021\_034 (B.M.); and CzechNanoLab Research Infrastructure, supported by MEYS CR (LM2018110). **Author contributions:** Conceptualization: P.J. Methodology: B.M., A.G., B.d.I.T., and P.J. Theoretical calculations: A.G., M.L., V.Š., P.J., and P.H. Experimental: B.M. and B.d.I.T. Funding acquisition: P.H. and P.J. Supervision: B.d.I.T., P.H., and P.J. Writing, original draft: B.M., A.G., B.d.I.T., P.H., and P.J. **Competing interests:** The authors declare that they have no competing interests. **Data and materials availability:** All data needed to evaluate the conclusions in the paper are present in the paper or the supplementary materials. Data can be found at Zenodo (41).

## SUPPLEMENTARY MATERIALS

science.org/doi/10.1126/science.abk1479  
Materials and Methods  
Supplementary Text  
Figs. S1 to S20  
Tables S1 to S3  
References (42–55)

24 June 2021; resubmitted 28 July 2021  
Accepted 20 September 2021  
10.1126/science.abk1479